INSTITUTE OF PHYSICS PUBLISHING JOURNAL OF PHYSICS: CONDENSED MATTER

J. Phys.: Condens. Matter **13** (2001) 10517–10532 PII: S0953-8984(01)28792-X

Photoelectron and x-ray holography by contrast: enhancing image quality and dimensionality

C S Fadley[1,2], M A Van Hove[1,2,3], A Kaduwela[1,6], S Omori[1,4,5], L Zhao[1,2] and S Marchesini[1]

[1] Materials Sciences Division, Lawrence Berkeley National Laboratory, Berkeley, CA 94720, USA
[2] Department of Physics, University of California, Davis, CA 95616, USA
[3] Advanced Light Source, Lawrence Berkeley National Laboratory, Berkeley, CA 94720, USA
[4] Institute of Industrial Science, University of Tokyo, Tokyo 106-8558, Japan
[5] Sony Corporation Semiconductor Network Company, 4-14-1 Asahi-cho, Atsugi, Kanagawa 243-0014, Japan

Received 13 September 2001
Published 9 November 2001
Online at stacks.iop.org/JPhysCM/13/10517

Abstract

Three forms of electron or x-ray holography 'by contrast' are discussed: they all exploit small changes in diffraction conditions to improve image quality and/or extract additional information. Spin-polarized photoelectron holography subtracts spin-down from spin-up holograms so as to image the relative orientations of atomic magnetic moments around an emitter atom. Differential photoelectron holography subtracts holograms taken at slightly different energies so as to overcome the forward-scattering problem that normally degrades the three-dimensional imaging of atoms, particularly for emitter atoms that are part of a bulk substrate environment. Resonant x-ray fluorescence holography also subtracts holograms at slightly different energies, these being chosen above and below an absorption edge of a constituent atom, thus allowing the selective imaging of that type of atom, or what has been referred to as imaging 'in true colour'.

1. Introduction

The holographic reconstruction of atoms in solids, including surfaces, interfaces and bulk materials, produces real-space images that locate individual atoms in the immediate neighbourhood of selected 'source' atoms [1–14], often to within a fraction of an Ångström. Here we will consider two types of outgoing waves that produce the holograms: photoelectrons and fluorescent x-rays, as produced via core-level excitations. Because such holograms and their associated images are produced by element-specific core processes, a key and well-recognized advantage of such holographies is that they are source-atom specific. That is, the

[6] Present address: California Air Resources Board, Sacramento, CA 95814, USA.

local environment of each type of atom in a complex system can be determined separately. However, such imaging does not readily provide the chemical or magnetic nature of the neighbour atoms. Also, the accuracy of the imaging, particularly with photoelectrons, is limited by effects such as the anisotropy of atomic scattering factors (with forward scattering a major obstacle), multiple scattering and truncation of the experimental data.

By contrasting holographic images measured under slightly different conditions, it is possible to obtain additional information, such as magnetic structure and chemical differentiation, and also to improve the quality of 'normal' holographic images.

This paper describes three methods of such 'holography by contrast'. In spin-polarized photoelectron holography (SPPH) [15] holograms measured with spin-up and spin-down electrons are subtracted from one another to produce a map of the relative orientations of magnetic moments in the neighbourhood of an atom emitting photoelectrons. In differential photoelectron holography (DPH) [16], one exploits the fact that the atomic forward-scattering (FS) peak varies only slowly with energy, such that another difference of holograms, this time at slightly different energies, is found to largely eliminate disruptive FS effects in imaging atoms. In resonant x-ray fluorescence holography (RXFH) [17], one uses the rapid change of the x-ray scattering factors near an absorption edge to selectively image individual chemical neighbours in a compound material.

Before proceeding to specific examples for each case, we note for clarity that a method called 'derivative' PH has been proposed by Chiang and co-workers [18], and this also is based on measurements of photoelectron intensity in slightly different conditions (at two nearby energies). However, the purpose there is to eliminate uncertainties in the experimental intensities I due to the variation of experimental conditions, by first taking logarithmic derivatives $[\partial I/\partial k]/I$ that are then reintegrated into 'self-normalized' intensities; after that step, the holographic reconstruction is 'normal'.

Various reconstruction algorithms [3, 4, 6] and measurement methods [19] have been proposed for photoelectron and x-ray fluorescence holography, many of which are represented by the formula

$$U(\boldsymbol{r}) = \left| \int W\chi(\boldsymbol{k}) \exp[-\mathrm{i}kr + \mathrm{i}\boldsymbol{k}\cdot\boldsymbol{r}]\,\mathrm{d}^3k \right|^2 \tag{1}$$

where U is the image intensity at position $\boldsymbol{r}$, $\chi(\boldsymbol{k}) = (I(\boldsymbol{k}) - I_0)/I_0$ is the normalized hologram based on intensities measured over three-dimensional $\boldsymbol{k}$ space, I_0 is the intensity in the absence of any scattering, and the function or operator W permits describing the difference between algorithms, with $W = 1$ in the original multi-energy formulations [3]. The three methods to be described in the following will start from this basic formula, and deviate from it in different ways.

As a general comment, we note that photoelectron holography involves very strong electron–atom scattering and thus very easily measured modulations in $\chi(\boldsymbol{k})$ that can reach $\pm 30\%$. This strong scattering is nonetheless not ideal for holography, in that it is also very anisotropic and at higher energies above about 300 eV also strongly peaked in the forward direction; it also leads to multiple scattering effects that can distort images or produce artefacts. Multiple-energy images based on equation (1) can improve the image quality and suppress multiple scattering effects, but scattering anisotropy and phase shift effects may remain. X-ray fluorescence holography by contrast involves very weak x-ray-atom scattering and much more difficult to measure modulations in $\chi(k)$ of typically a few tenths of a per cent. However, the weak nature of the scattering leads to holograms that are much more ideal, and to correspondingly more accurate atomic images.

2. Spin-polarized photoelectron holography (SPPH)

There is great interest in studying near-surface magnetism in various types of nanostructures for which magnetic order may be significantly different from that of the corresponding bulk materials. Spin-polarized photoelectron diffraction (SPPD) without direct imaging has already proven capable of detecting changes in short-range magnetic order as a given transition temperature is crossed for both antiferromagnets [20] and a ferromagnet [21], but adding three-dimensional imaging to such measurements would render them much more powerful. It has previously been demonstrated theoretically [15] that it should be possible to image short-range magnetic structure by means of photoelectron holography in which the electron spin is resolved.

The method relies on the difference in the scattering of spin-up versus spin-down electrons by atoms that carry a net spin magnetic moment. The primary interaction involved is thus exchange between the photoelectron and the unpaired valence electrons on the magnetic atom, although spin–orbit effects also may have to be considered for the most accurate description, especially for scattering from heavier atoms. The photoelectron spin can be resolved simply by exploiting the energy separation between multiplet-split core levels in transition metal compounds or ferromagnetic metals. This constitutes an internally referenced source of spin-polarized photoelectrons, giving magnetic moment orientations relative to that of the source atom. Adding an external spin detector and/or exciting spin–orbit split levels with circularly polarized radiation [22] provides the further possibility of making externally referenced measurements, giving absolute magnetic orientations in the laboratory frame.

If we measure separately the two holograms $\chi_\uparrow(\boldsymbol{k})$ and $\chi_\downarrow(\boldsymbol{k})$ for the two different spin orientations, and if $U_\uparrow(\boldsymbol{r})$ and $U_\downarrow(\boldsymbol{r})$ are their respective reconstructed images using 'normal' holographic methods, we can define two separate difference images that focus on just the spin-dependent aspects of the scattering:

$$\Delta(\boldsymbol{r}) = U_\uparrow(\boldsymbol{r}) - U_\downarrow(\boldsymbol{r}) \tag{2}$$

and

$$\Delta'(\boldsymbol{r}) = \left| \int_k \exp(-\mathrm{i}kr) \iint_{\hat{k}} \exp(\mathrm{i}\boldsymbol{k}\cdot\boldsymbol{r}) [\chi_\uparrow(\boldsymbol{k}) - \chi_\downarrow(\boldsymbol{k})] k^2 \,\mathrm{d}k \sin\theta_k \,\mathrm{d}\theta_k \,\mathrm{d}\varphi_k \right|. \tag{3}$$

The latter is the normal three-dimensional holographic transform of equation (1), but now applied to the difference of the spin-up and spin-down holograms.

The expectation is that $\Delta(\boldsymbol{r})$ will show signals of opposite sign at atomic locations with opposite magnetic moment. It should also show no signal at the locations of non-magnetic atoms. Because of the overall absolute value, the second image, $\Delta'(\boldsymbol{r})$, should not show spin-up versus spin-down sensitivity, but should nonetheless show the location of magnetic moments, while again suppressing non-magnetic atoms.

The potential of this method is illustrated in figure 1 for a simulated experiment for a small cluster representing a MnO(001) surface (figure 1(a)) [15, 23]. Atomic magnetic moments are shown in figure 1(a) as cones pointing up or down. Spin-up and spin-down photoelectrons are emitted from the central Mn^{2+} atom, and they can side-scatter from both O and Mn atoms in the same plane so as to yield two different sets of holograms. These holograms have been calculated with full multiple scattering and spin-dependent potentials [24][7]. Spin-up electrons scatter from spin-down Mn^{2+} atoms without the normal exchange potential that is included in the scattering of electrons from same-spin Mn^{2+} atoms, and therefore, two separate sets of phase shifts are needed to calculate the electron scattering. The potential is slightly more attractive

[7] MSCD photoelectron diffraction program package from http://electron.lbl.gov/mscdpack/mscdpack.html.

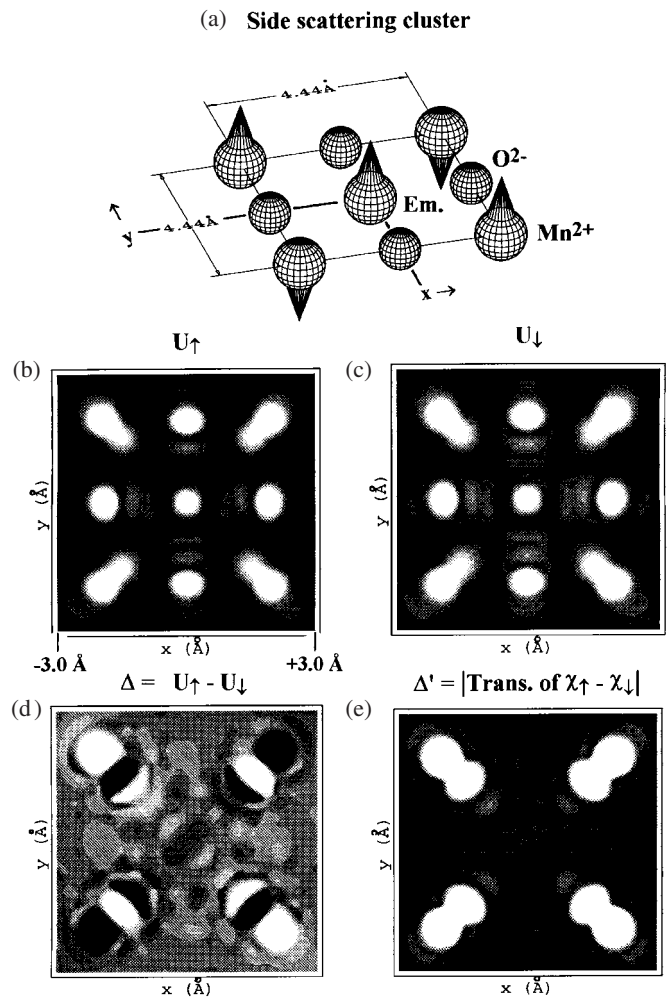

Figure 1. Theoretical simulation of spin-polarized photoelectron holography (SPPH): (a) a nine-atom cluster representing the (001) surface of MnO, with an emitter in its centre and eight side-scattering Mn and O neighbours around it; (b), (c) normal holographic images $U_{\uparrow}(\boldsymbol{r})$ and $U_{\downarrow}(\boldsymbol{r})$ generated for the two different photoelectron spins using ten energies between 127 and 278 eV; (d) spin-sensitive holographic image $\Delta(\boldsymbol{r})$; according to equation (2). (e) Spin-sensitive holographic image $\Delta'(\boldsymbol{r})$ according to equation (3).

when the spin of the photoelectron and the net spin of the Mn atom are parallel. Holograms were calculated at ten energies between 127 and 278 eV, so as to be able to take advantage of the well known image improvements possible with multi-energy imaging [2, 6, 7]. An important detail in using the spin-dependent image functions in equations (2) and (3) in the most unambiguous way is that the calculations were performed at the same final electron energy for spin-up and spin-down electrons, so that the spatially dependent diffraction conditions remain the same (i.e. same photoelectron wavelength). In practice, this would require an experiment to shift the incoming photon energy by an amount corresponding to the difference in the two spin-resolved photoelectron peaks (e.g., about 6.0 eV for the Mn 3s multiplets in the MnO case considered here) between the spin-up and spin-down measurements, thus again requiring a tunable synchrotron radiation photon source.

Figures 1(b) and (c) show standard multi-energy holographic reconstructions (via equation (1) with $W = 1$) and produced with spin-up and spin-down electrons, respectively. They look much alike, due to the relatively small effect of the exchange potential (5–15% of the total effective scattering potential), and both image the nine atoms of the cluster. Their difference image $\Delta(\boldsymbol{r})$ (equation (2)) is shown in figure 1(d): the Mn^{2+} atoms are imaged with opposite contrast, reflecting their opposite magnetic moments, while the oxygen atoms are effectively suppressed, as expected. Phase variation across the Mn^{2+} images produces oscillations in sign, but it is nonetheless clear that the two pairs of Mn scatterers have opposite orientation. To establish the orientation of the magnetic moments on the scatterers relative to that on the emitter would require further work, e.g. in comparing experimental and theoretical images. The second type of difference image $\Delta'(\boldsymbol{r})$ (equation (3)) shown in figure 1(e) also confirms expectations: it images the magnetic moments without being sensitive to their orientation, and omits the non-magnetic atoms.

Beyond the two simple imaging functions considered here for SPPH, Timmermans *et al* have also discussed from a theoretical point of view more detailed vectorial methods, including spin–orbit contributions to the difference of the spin-up and spin-down photoelectron fluxes [25]. These methods also show promise for even more precise studies of short-range magnetic order in future experimental work.

Thus, spin-polarized photoelectron holography represents an intriguing and challenging experimental possibility for the future, but one well matched to the new synchrotron radiation sources that are now becoming available. Possible applications would be to some of the strongly correlated materials and to complex magnetic alloys, for which the interaction between short-range and long-range magnetic order is thought to play a strong role in producing intriguing properties.

3. Differential photoelectron holography (DPH)

From the first papers on photoelectron holography, it has been clear that the strong electron–atom scattering involved was both a blessing in producing large holographic oscillations and easily measured holograms, and a curse in yielding very anisotropic scattering factors that are strongly peaked in the forward direction at higher energies above a few hundred eV [2, 6, 23]. Since the ideal scattering factor for holography would be weak and isotropic, photoelectron holographic images can often suffer distortions and peak shifts. Some of these aberrations can be corrected by using a sufficiently large multi-energy data set, but it has still proven particularly difficult to image bulk-like atoms that are present in the first few layers below a surface, as recently illustrated for the case of bulk atom emission from W(110) [7].

To overcome the poor imaging quality associated with strong and anisotropic forward scattering (FS) of electrons, a new approach called 'differential holography' has been proposed. This proceeds simply by replacing χ in equation (1) by its derivative with respect to the magnitude of the photoelectron wavevector $\boldsymbol{k}$ (or equivalently by setting $W = \partial/\partial k$) or more conveniently by a numerical difference between two χ at slightly different energies ($\delta\chi = \chi(k+\delta k) - \chi(k)$). FS effects can be greatly suppressed via this method. This method has been applied to both experimental and theoretical multi-energy holograms for Cu 3p emission from Cu(001), and results in images that are improved over prior work in several respects. Applications of this approach in other electron-based holographies also appear possible.

The principle of DPH is as follows: we consider the single-scattering expression of the hologram χ for an emitter–scatterer pair spaced by a vector $\boldsymbol{r}$ [26]:

$$\chi(\boldsymbol{k}) = \frac{I - I_0}{I_0} \approx \frac{2|f(k, \theta_r^k)|}{r} \cos\left[kr(1 - \cos\theta_r^k) + \varphi(k, \theta_r^k)\right] \tag{4}$$

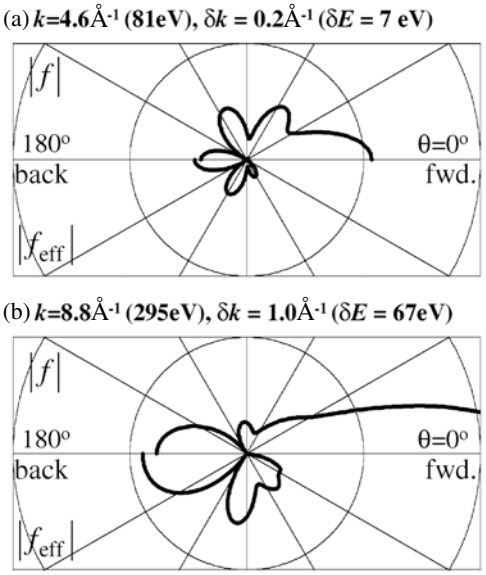

Figure 2. Comparison of the usual scattering amplitude $|f|$ and the effective scattering amplitude of differential holography $|f_{\rm eff}|$, calculated for Cu–Cu nearest neighbours ($r = 2.56$ Å) as a function of scattering angle θ_r^k for two different sets of k and δk in taking the differential of χ: (a) $k = 4.6$ Å^{-1} (81 eV), $\delta k = 0.2$ Å^{-1} (7 eV) and (b) $k = 8.8$ Å^{-1} (295 eV), $\delta k = 1.0$ Å^{-1} (67 eV). The final strong FS data points of $|f|$ at the right of panel (b) are truncated. We have confirmed numerically that equation (3) is a good approximation even in the case of (b), where δk has a larger fractional value.

where I_0 is the intensity that would be observed without atomic scattering and φ is the scattering phase. If δk is sufficiently small so that $\delta|f|/|f| \ll 1$, where $\delta|f|$ is the change in $|f|$, the difference of two holograms at $k_\pm = k \pm \delta k/2$ can be written in a form similar to equation (4):

$$\delta\chi(\boldsymbol{k}) = \chi(k_+\hat{\boldsymbol{k}}) - \chi(k_-\hat{\boldsymbol{k}}) \approx -\frac{2|f_{\rm eff}|}{r}\sin\left[kr\left(1-\cos\theta_r^k\right) + \bar{\varphi}\left(k,\theta_r^k\right)\right] \qquad (5)$$

where the direction $\hat{\boldsymbol{k}}$ is defined by angles θ and ϕ, the 'effective' scattering amplitude is defined as $|f_{\rm eff}| = 2|f|\sin\left[\delta kr\left(1-\cos\theta_r^k\right)/2 + \delta\varphi/2\right]$, and $\bar{\varphi}$ is the average of the φ at $k_\pm$. In the FS region ($\theta_r^k \to 0$), $|f_{\rm eff}|$ is thus very small, approaching zero in the limit of $\delta\varphi \to 0$. If δk is also small, $|f_{\rm eff}|$ is proportional to r; thus, DPH not only suppresses the FS effects, but also enhances the imaging of distant atoms. However, $\bar{\varphi}$ still remains in the sinusoidal holographic oscillation of equation (5), and this could be the origin of small image position shifts.

In figure 2, $|f|$ and $|f_{\rm eff}|$ are plotted as a function of θ_r^k for Cu–Cu nearest neighbours ($r = 2.56$ Å) and two choices of energy and energy difference. For $k = 4.6$ Å^{-1} and $\delta k = 0.2$ Å^{-1}, $|f_{\rm eff}|$ is significant only in the region of $\theta_r^k > \sim 90°$. Therefore, the imaging of side-scattering (SS) and back-scattering (BS) atoms is expected, while it will be difficult for this case to image FS atoms. On the other hand, for $k = 8.8$ Å^{-1} and a larger fractional $\delta k = 1.0$ Å^{-1}, $|f_{\rm eff}|$ is significant not only in the BS region but also in the range of $\theta_r^k \sim 30$–$90°$. Since it is well known that near-neighbour FS diffraction fringes extend out beyond 30° [26,27], we might expect the latter choice to also permit imaging FS atoms. In this way, the relative sensitivity of DPH to SS and FS atoms can be 'tuned' by selecting the range and step width of k scans.

To demonstrate DPH experimentally, we have applied the method to measured photoelectron holograms [16]. Photoelectron spectra for Cu 3p emission were measured at 25 energies over $k = 4.5$–9.3 Å^{-1} ($E_k = 77$–330 eV) with a constant step of $\delta k = 0.2$ Å^{-1} (corresponding to $\delta E_k = 7$–14 eV), along 65 different directions over a symmetry-reduced 1/8 of the total solid angle above the specimen, and with a polar angle range from $\theta = 0°$ (surface normal) to 70°. A total of 1625 distinct intensities were thus measured.

The photoelectron intensity $I(\boldsymbol{k} = k, \theta, \phi)$ was fitted by low-order polynomials with three variables to obtain the smooth background intensity I_0 [7,28]. Three kinds of χ were obtained from this fitting: $\chi_{\rm A}$ by fitting a scanned-angle pattern $I_k(\theta, \phi)$ at each fixed k [5], χ_B by

fitting a scanned-energy curve $I_{\hat{\boldsymbol{k}}}(k)$ at each fixed direction $\hat{\boldsymbol{k}}$ [6] and χ_C by fitting to the full data set of $I(k, \theta, \phi)$ at once, with the last being the most accurate from an *a priori* point of view [7]. The k-differences from χ_C were also used for DPH in what we will term method D (i.e. $\chi_D = \delta\chi_C$ as defined in equation (5)). The proper method of I_0 subtraction has been the origin of some controversy concerning the fidelity of reconstructed images, and so warrants a little more discussion here [9]. It has been suggested [9] that method B has an advantage over method A in that low-frequency oscillations due to FS events in $I_{\hat{\boldsymbol{k}}}(k)$ are automatically removed. However, this also means that the I_0 from method B inherently deviates from the true I_0 defined as the intensity without scattering, especially in the FS direction. In addition, since each $I_{\hat{\boldsymbol{k}}}(k)$ is independently normalized without considering the continuity of χ in the whole sampled $\boldsymbol{k}$ space, method B could degrade holographic fringes in $I_k(\theta, \phi)$. Similarly, method A could degrade holographic oscillations in $I_{\hat{\boldsymbol{k}}}(k)$. In contrast, method C takes into account the continuity of χ over the whole data set, but the FS peaks remain in χ_C. Method D (= DPH with χ_C) should suppress these forward scattering effects. Thus, a comparison of methods A–D is of interest in general from the point of view of holographic methodology and it also provides a critical test for the efficacy of DPH in reducing FS effects. The simple original transform was used for all four data sets; but to avoid spurious features due to the abrupt truncation of the integral in equation (1), W was taken to be the product of a Gaussian function of k and a Hanning function $\cos^2\theta$, with an additional multiplication by r to make atoms at larger distances more visible.

Figure 3 shows cross atomic images reconstructed with the four methods in the vertical (100) plane of Cu(001), with methods A–D being applied to experimental data in parts (a)–(d), respectively, and methods C and D being applied to an accurate multiple-scattering simulation of the experimental results in parts (e) and (f), respectively. First considering methods A–C which are different approaches to standard photoelectron holography, we see the qualitatively expected results that method A retains strong FS features, requiring a large enhancement factor of 46× in the bottom part of the image to display BS atoms of types 1 and 3 (figure 3(a)), that method B indeed suppresses these features strongly, with enhancement by 5× now being necessary in the top part of the image to see some SS atoms of type 4 (figure 3(b)); and that method C is intermediate between A and B in requiring somewhat less enhancement (by 29× in experiment and 49× in theory) in the lower part of the image to see some BS and SS atoms (figures 3(c), (e)). Note also that methods A and C also possess strong elongated images of the FS atoms of type 6, as seen in a prior application of method A to Cu(001) [5].

Turning now to DPH in figures 3(d), (f), we find method D to be the most robust for imaging both SS and BS atoms (and to some degree also FS atoms of type 6). All of the BS and SS atoms of types 1, 2, 3 and 4 are seen clearly in these DPH images, with only a small enhancement factor of 5× being required in the top half of the image (as with method B, but with superior image quality to it). Comparing the positions of these images in DPH with the known atomic positions in Cu, there are shifts in position of approximately 0.1 Å for type 1, 0.6 Å for 2, and 0.3 Å for 3. Such peak shifts relative to the true atomic positions, as observed in all methods, can be attributed to the neglect of corrections for both the scattering phase and the inner potential, which have not been included here.

For comparison with experiment, we have also performed multiple-scattering simulations of $I(\boldsymbol{k})$, using a cluster method [24]. The theoretical I_0 was obtained simply as the square of the zeroth-order wave function without scattering. Images reconstructed from the theoretical χ and $\delta\chi$ via methods C and D are shown in figures 3(e) and (f). The main features in figures 3(c) and (d) are well reproduced by our simulations, although the artefacts between the images of atoms 3 are much stronger in experiment for method C, and the relative intensity in the region of FS atom 6 is stronger in experiment for method D.

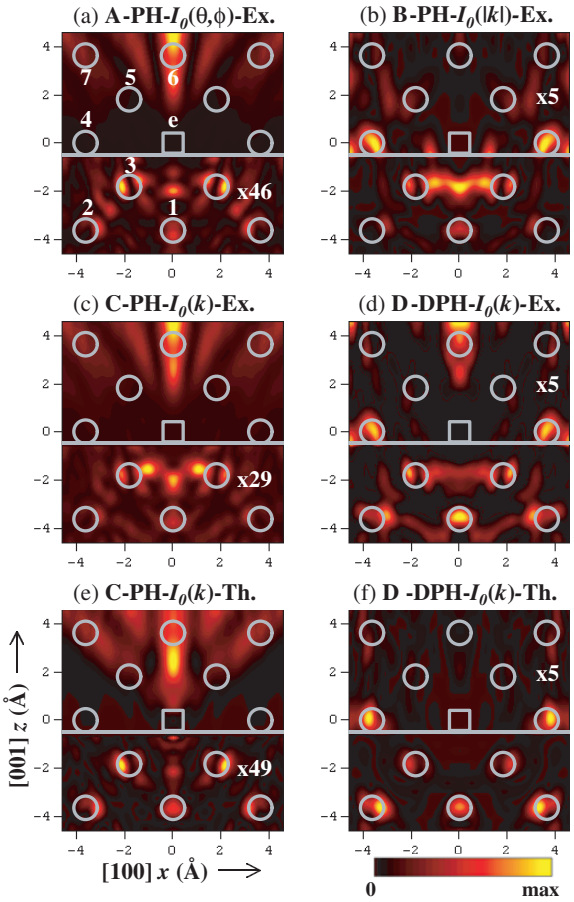

Figure 3. Atomic images in the vertical (100) plane of Cu(001) reconstructed from Cu 3p holograms obtained by normal photoelectron holography (PH, methods A–C) and differential photoelectron holography (DPH, method D), as described in the text. The emitter and scatterer positions are indicated by squares and circles, respectively, and various near-neighbour atoms are numbered. Image intensities above or below $z_c = -0.5$ Å have been rescaled by the factor shown in each panel, with this factor being determined so as to make the maximum intensities above and below z_c equal. *Experimental images*: (a) image obtained by method A: normal holography via equation (1) with I_0 determined by fitting its angular variation at each k value. (b) Image obtained by method B: normal holography with I_0 determined by fitting its k variation along each direction. (c) Image obtained by method C: normal holography with I_0 determined by fitting both its angular and k variations. (d) Image obtained by method D: differential holography with I_0 determined by fitting both its angular and k variations. *Theoretical images*: (e) as (c) but theoretical. (f) As (d) but theoretical.

(This figure is in colour only in the electronic version)

Figures 4 and 5 further show three-dimensional representations of the experimental images in figures 3(a)–(d), with figure 4 first indicating clearly that DPH can effectively image approximately 20 BS and SS atoms around a given emitter e and up to two planes below it. In this image, we find in addition to the atoms of types 1–4 and 6 in figure 3, two other types of near-neighbour BS and SS atoms located in the vertical (110) plane (denoted 2′ and 4′ and situated in the same horizontal layers as 2 and 4, respectively). All of these atoms are

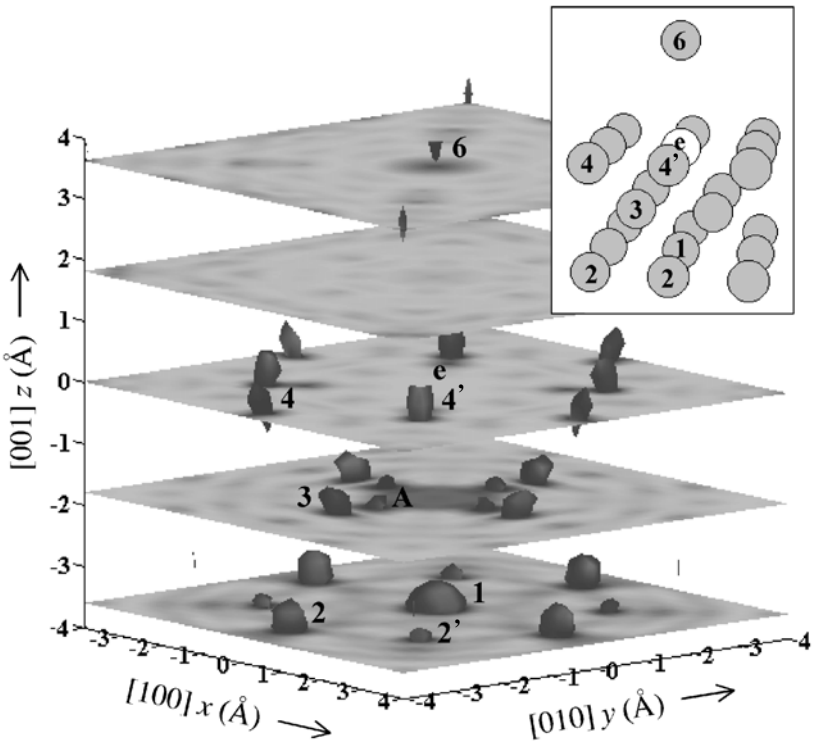

Figure 4. Three-dimensional Cu(001) atomic image reconstructed from the experimental holograms by method D—differential holography with a 3D I_0 function. Image intensities above $z_c = 0.5$ Å have been multiplied by a factor of 4, and isosurfaces at 50% of the maximum intensity are shown together with five slices at $z = 0$ (the emitter plane), ± 1.81 (the first nearest layers) and ± 3.62 Å (the second nearest layers). Reconstructed forward-, side- and back-scattering atoms are numbered, and the corresponding atoms in the crystal model are indicated in the inset. Only the four features labelled A inside the atomic peaks 3 are weak artefacts that cannot be connected with a specific atom.

reasonably well imaged, with only a few, such as 2, being significantly shifted in position, but most within a few tenths of an Å of the correct positions in all directions. Even though four weaker artefacts (labelled A in figure 4) are observed at radii inside of the positions of atoms 3, the three-dimensional image quality is much higher than any of the previous PH images of bulk substrate emission [5, 7].

The experimental images in figure 5 permit a direct comparison of methods A–D in three dimensions, and confirm our earlier comments concerning the relative importance of back, side, and FS atoms, and the superiority of the DPH image.

In conclusion, DPH provides an effective method for reducing FS artefacts in images and significantly improves the imaging of back and SS atoms. With an appropriate choice of the energy difference and $\boldsymbol{k}$-space sampling used, FS atoms should also be imaged more accurately by this method. This method should also be helpful in reducing FS artefacts in other types of electron holography in which energy can be stepped in a controlled way, as e.g. in Kikuchi [9] or LEED [10] holography.

Finally, we for completeness point out briefly a couple of other promising methods that have been suggested by other groups for reducing FS effects and improving images in photoelectron holography.

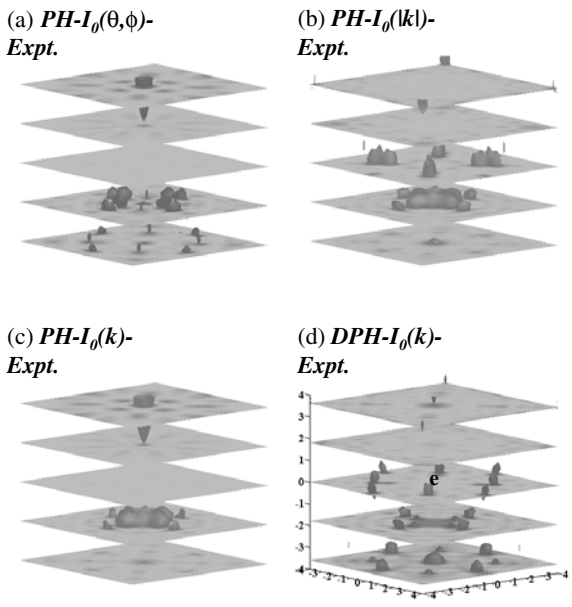

Figure 5. As figure 4, but for all four experimental image cases considered in figures 3(a)–(d).

- *Near-node photoelectron holography*. In this method, as suggested by Greber and Osterwalder [19] and recently demonstrated experimentally by Wider *et al* [29], the experimental geometry is chosen so that the polarization vector is nearly perpendicular to the electron emission direction. Thus, if the photoelectric cross section is roughly p-like (as is rigorously true for dipolar emission from an s-subshell), the strength of the wave emitted in the FS direction is reduced, and significant improvement in imaging BS, SS and FS atoms has been seen in images produced by Al 2s emission from Al(111) [29]. This method requires using a special experimental geometry, and is most effective for s-subshell emission, although many non-s subshells have roughly p-like cross sections at higher photon energies.
- *Circular dichroism in photoelectron holography*. In one method of this type suggested by Daimon *et al* [30], advantage is taken of the fact that photoelectron diffraction features tend to be 'rotated' to the left or right if excited by left or right circularly polarized radiation [31]. The degree of rotation is in first approximation inversely proportional to the distance to the scatterer producing a given peak, and thus a kind of stereoscopic image of the near-neighbour environment can be obtained [30]. In another variant of this, it has been pointed out by Oelsner and Fecher [32] that taking a difference of two holograms obtained with left and right circularly polarized radiation and using this difference in an inversion formula analogous to equation (5) can produce accurate single-energy atomic images, with the theoretical reasons for this being discussed in some detail.

4. Resonant x-ray fluorescence holography (RXFH)

Since Szöke's original suggestion of x-ray fluorescence holography (XFH) as one of the possible inner-source holographies [33], the technique has been pursued first via theoretical feasibility studies [11], and then developed experimentally in both normal [34] and inverse modes [35]. Review articles discussing the first experiments and some likely future directions have also appeared [36, 37]. As examples of the current status of XFH, more recent work

has demonstrated the ability to image up to 100 atoms in a volume of (10 Å)^3 surrounding a given emitter and to see a low-Z atom in the presence of a high-Z atom [38], and to image the local environment in a quasi-crystal lacking long-range periodicity [39]. It has also been shown previously that the local environment of a dopant at the $\sim$0.1% level can be successfully imaged in a semiconductor lattice [40].

Even though XFH in either of the two original modes thus offers a powerful method to probe the local atomic structure around a given atom, it still lacked a key ingredient of the 'ideal' probe: the technique may be element-specific for the central atom in the structure, but there was no simple way to determine the near-neighbour atomic identities. Use can be made of the differences in x-ray scattering strengths between different atoms, but this is only unambiguous when the atomic numbers are very different. It has thus recently been proposed, based on theoretical simulations, to perform resonant x-ray fluorescence holography (RXFH) so as to permit the direct imaging of atoms of a preselected type in solids [17]. This new variant of XFH thus should provide a unique way to determine chemical order and disorder around a given type of atom, through spectroscopic 'true colour' selection. RXFH thus represents an important improvement to XFH in the inverse mode (often termed multi-energy x-ray holography (MEXH) [12]), which should enable the direct discrimination of different atoms in reconstructed images even for the most difficult cases where the atomic numbers of elements involved are very close together.

The principle of RXFH is discussed here with the example of a binary compound with close atomic numbers. As noted above, a considerable amount of experimental work on MEXH has so far demonstrated that atomic images of this kind of crystal can be obtained with reasonable accuracy and resolution without special difficulties by using state-of-the-art facilities based on third-generation synchrotron sources [41]. Thus, it should be technically possible to obtain additional information on the chemical identities of such atomic images that can lead to more complete structural characterization of the crystal.

To illustrate the method, we first label the central atom of the reconstructed images to be of type A: this is the fluorescing atom. The incident photon energy is then tuned across a strong core absorption resonance of some other atom in the lattice that we label B, so that the scattering factor of atom B changes rapidly. The anomalous dispersion for element B which occurs in passing over the absorption resonance is then used to image only atoms of type B. In RXFH, holograms are thus measured at a few energies in the vicinity of the absorption edge of element B, $E^{\mathrm{B}}_{\mathrm{abs}}$.

As an example, we consider the compound $FeNi_3$ with A = Fe and B = Ni. Figure 6 shows the real and imaginary parts of the corresponding scattering factors $f^{\mathrm{A}}(0)$ and $f^{\mathrm{B}}(0)$ in the FS direction, in the vicinity of the K absorption edge of Ni. A choice of three energies for RXFH is also indicated, with these spanning a small energy region ($\Delta E = 197$ eV) around $E^{\mathrm{B}}_{\mathrm{abs}}$ (8333 eV). It is seen that as the energy is swept across $E^{\mathrm{B}}_{\mathrm{abs}}$, the atomic scattering factor $f^{\mathrm{B}}(0)$ of element B changes drastically, while $f^{\mathrm{A}}(0)$ remains nearly constant, because $E^{\mathrm{A}}_{\mathrm{abs}}$ is far outside of this energy range (but still close enough to induce Fe Kα radiation sufficient for realistic experiments).

The portions of an *incident* x-ray wave scattered by atoms constitute the object waves in this inverse form of x-ray fluorescence holography, and they interfere with the unscattered portion of the incident reference-wave to give rise to an interference field at atom A inside the crystal. Since $E > E^{\mathrm{A}}_{\mathrm{abs}}$ (7112 eV), the total strength of the wave field at the atomic positions of element A can be measured by integrating fluorescent x-rays from A over a large solid angle. Thus, an x-ray hologram with the central atom A can be obtained at each energy by recording the intensity $I(k, \theta, \phi)$ of fluorescent x-rays as a function of the x-ray incident direction and then normalizing I by the smooth background intensity I_0, numerically derived

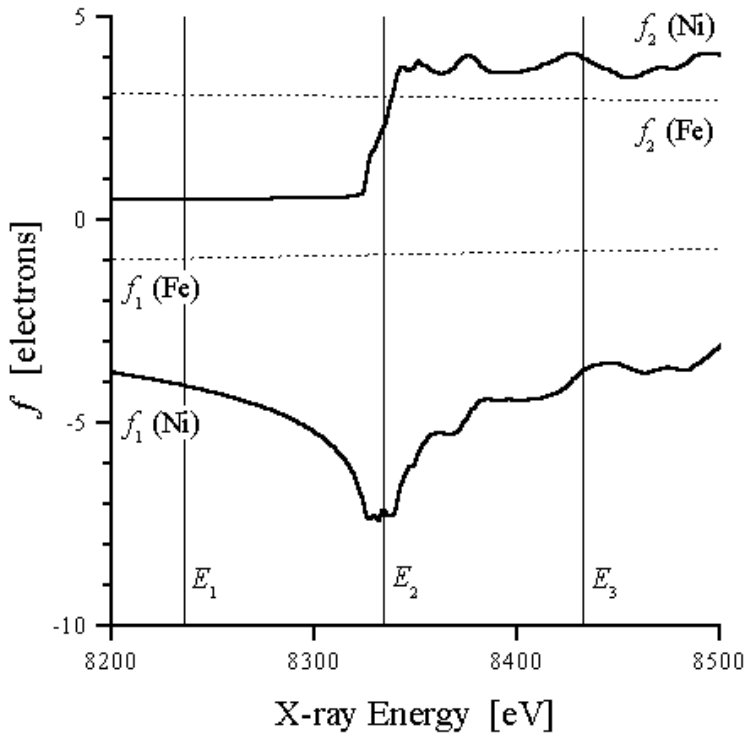

Figure 6. X-ray scattering factors in the forward direction for Fe (dotted lines) and Ni (solid curves) atoms as a function of x-ray energy around the K edge of Ni. The real and imaginary parts are denoted as f_1 and f_2, respectively, and the real parts are shifted down by the atomic numbers. Three energies used for the MEXH and RXFH simulations, E_1, E_2 and E_3, are indicated by vertical solid lines and correspond to 8235 eV ($k = 4.17$ Å^{-1}), 8334 eV ($k = 4.22$ Å^{-1}) and 8433 eV ($k = 4.27$ Å^{-1}), respectively.

from I, as $\chi\,(k, \theta, \phi) = (I - I_0)\,/I_0$. The contribution to the recorded holograms from atoms of type A can be largely cancelled out by taking the difference of two holograms at energies close to $E^{\mathrm{B}}_{\mathrm{abs}}$, while such a differential hologram will receive relatively strong contributions from atoms B resulting from the rapid change in f^{B}.

To more quantitatively develop the holographic transform appropriate for RXFH, the mathematical expression for the differential x-ray hologram in MEXH [17] is discussed next. For simplicity, we consider the normalized hologram χ for a scatterer–absorber pair, which is equivalent to equation (4) but in slightly different form:

$$\chi\,(\boldsymbol{k}) = \frac{f\left(k, \theta^{\boldsymbol{k}}_{\boldsymbol{R}}\right)}{R} \exp\left[\mathrm{i}kR - \mathrm{i}\boldsymbol{k}\cdot\boldsymbol{R}\right] + \mathrm{c.c.} \tag{6}$$

where $\boldsymbol{R}$ is the scatterer position, and $\theta^{\boldsymbol{k}}_{\boldsymbol{R}}$ is the scattering angle between $\boldsymbol{k}$ and $\boldsymbol{R}$. The difference between two holograms at $k_{\pm} = k \pm \delta k/2$ is given in a form similar to equation (6) but using an effective scattering factor, just as that discussed for DPH above [16, 27]:

$$\delta\chi\,(\boldsymbol{k}) = \frac{f^{\mathrm{eff}}\left(k, \theta^{\boldsymbol{k}}_{\boldsymbol{R}}\right)}{R} \exp\left[\mathrm{i}kR - \mathrm{i}\boldsymbol{k}\cdot\boldsymbol{R}\right] + \mathrm{c.c.} \tag{7}$$

and with a more accurate form for the effective scattering factor due to the possibility now of

a non-negligible change in f in crossing a resonance:

$$f^{\text{eff}}\left(k,\theta_{\boldsymbol{R}}^{\boldsymbol{k}}\right)=\delta f\exp\left[\mathrm{i}\frac{\delta k}{2}\left(R-\hat{\boldsymbol{k}}\cdot\boldsymbol{R}\right)\right]+2\mathrm{i}f\left(k_{-},\theta_{\boldsymbol{R}}^{\boldsymbol{k}}\right)\sin\left[\frac{\delta k}{2}\left(R-\hat{\boldsymbol{k}}\cdot\boldsymbol{R}\right)\right]. \tag{8}$$

Equation (8) shows two contributions to $\delta\chi$. The first is due to the change in the scattering factor δf, which can appear even for the smallest δk if there is any abrupt change in f, as at the absorption edge: this term is exploited in RXFH. The second contribution is significant even when δf is nearly zero as long as δk is finite: as discussed earlier, it is used in DPH. In fact, $f^{\text{eff}}=\delta f$ in the limit of $\delta k\to 0$, so that $\delta\chi$ contains structural information about only the resonant species, as measured relative to the central A atom.

In trying to do element-specific imaging via this approach, we first note that the form of the x-ray-atom scattering factor is in general

$$f\left(k,\theta_{\boldsymbol{R}}^{\boldsymbol{k}}\right)=f_{\text{Atom}}\times f_{\text{Thomson}}=\left[f_0\left(\theta_{\boldsymbol{R}}^{\boldsymbol{k}}\right)+f_1-\mathrm{i}f_2\right]\times f_{\text{Thomson}}(\theta_{\varepsilon}^{k}) \tag{9}$$

where f_{Atom} is the atomic scattering factor, f_{Thomson} is the polarization-dependent Thomson scattering factor, θ_{ε}^{k} is the angle between the scattered x-ray and the light polarization (here assumed linear), f_0 is the tabulated atomic form factor, and f_1 and f_2 are the real (refractive) and imaginary (absorptive) parts of the atomic scattering factor, respectively [42]. The terms f_1 and f_2 are the only quantities which vary strongly with photon energy. One can thus try to exploit the change in f_1, the change in f_2, or both. It is clear from figure 6 that the variations are more gradual in the real part than in the imaginary part, with f_1 showing a broad dip near the resonance that sets in before the K absorption edge for Ni is actually reached, and f_2 showing an abrupt jump right at the edge. To use the variation in the real part, one could use the relatively wide energy spacing shown in figure 6, and contrast holograms taken at one or two off-resonance energies with a hologram taken at the resonance energy. This choice appears to be better than trying to exploit the variation in the imaginary part. In this latter case, two energies should be chosen just below and above $E_{\text{abs}}^{\text{B}}$, so that $\delta f^{\text{A}}\approx 0$ and $\delta f^{\text{B}}\approx -\mathrm{i}\delta f_2^{\text{B}}$; while this scheme works in principle, it is found that a very high, but still realistic, signal-to-noise ratio would be required. Thus, although both approaches should probably work in future experiments, we will here focus on using the change in the real part, which appears somewhat easier to achieve in the laboratory.

In the three-energy case shown in figure 6, two differential holograms, $\delta\chi_1=\chi_2-\chi_1$ and $\delta\chi_2=\chi_3-\chi_2$, are obtained from normal holograms at the three energies. The two differential holograms are then summed for extra signal. However, since the change in the real part of the scattering factor f_1^{B} has opposite signs on either side of $E_{\text{abs}}^{\text{B}}$, the differences $\delta\chi_1$ and $\delta\chi_2$ also tend to change signs and would largely cancel out in the sum. Therefore we include a sign $\sigma(k-k_{\text{abs}}^{\text{B}})$ to compensate for this:

$$U\left(\boldsymbol{r}\right)=\int k^2\,\mathrm{d}k\,\sigma\left(k-k_{\text{abs}}^{\text{B}}\right)\int\delta\chi\left(\boldsymbol{k}\right)\exp\left[\mathrm{i}\boldsymbol{k}\cdot\boldsymbol{r}\right]\mathrm{d}^2\hat{\boldsymbol{k}} \tag{10}$$

where $\sigma\left(k-k_{\text{abs}}^{\text{B}}\right)=+1$ for $k>k_{\text{abs}}^{\text{B}}$ and $\sigma\left(k-k_{\text{abs}}^{\text{B}}\right)=-1$ for $k<k_{\text{abs}}^{\text{B}}$; here the first integral generalizes the summation to more energies, if desired. In this case, the changes δf_2^{B} in the imaginary parts above and below the edge are nearly equal (since E_2 is centred on the edge) so that their contributions nearly cancel out in equation (10). The overall resonant effect is mostly due to the change in the real part δf_1^{B}. Furthermore, that difference is comparable in magnitude to the normal atomic scattering factors of light elements such as C, N and O, with the last having recently been imaged by MEXH [38, 39]. By comparison, the contributions from atoms A are greatly reduced; thus, we have reason to believe that such an element-specific contrasted image should be achievable experimentally. It is also easy to show that if either f or f^{eff} is real, the real part of U has a negative peak at the atomic position [42]. Therefore, we

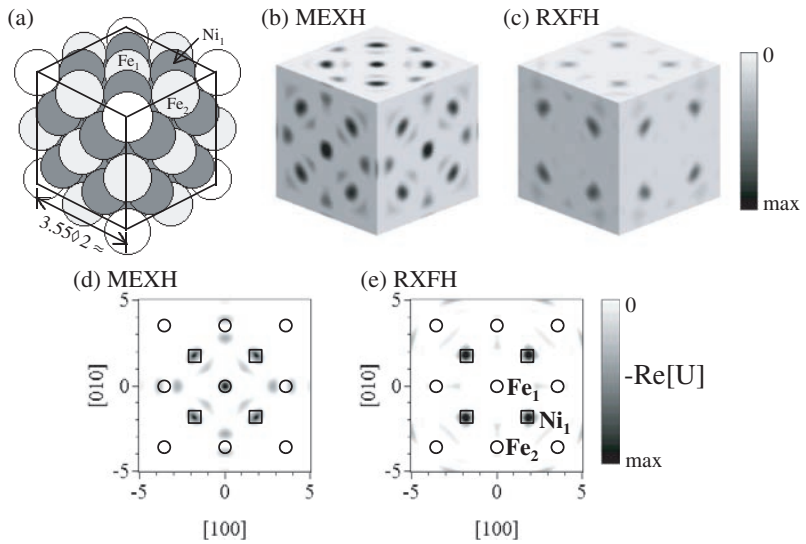

Figure 7. Comparison of multiple-energy x-ray holography (MEXH) and resonant x-ray fluorescence holography (RXFH) based on single-scattering simulations for the $FeNi_3$ crystal. (a) Crystal model of $FeNi_3$ corresponding to the reconstructed images in (b) and (c) and including eight unit cells with the lattice constant of 3.55 Å. The Fe and Ni atoms observed in (b) (marked as Fe_1, Fe_2 and Ni_1) are shown as thin and thick gray circles, respectively, while the Fe atoms not observed in (b) are shown as open circles. (b) Three dimensional reconstructed image from MEXH sliced along six {001} planes. (c) Corresponding image from RXFH. The fluorescing Fe atom is located at the centre of the cubes in (b) and (c). (d) Enlarged reconstructed image from MEXH in the (001) plane. (e) Corresponding enlarged image from RXFH. The true atomic positions of Fe and Ni atoms are shown as circles and squares, respectively, with some key atoms labelled.

have used the negative real part of $U = -\mathrm{Re}\,[U]$ for presenting the reconstructed images in the following, further showing only those parts of this image function that are positive to conform to theoretical expectations: thus, if Re [U] > 0, image $U = 0$, and if Re [U] < 0, U $= -$Re [U].

To quantitatively demonstrate RXFH, x-ray holograms were simulated for the $FeNi_3$ model crystal, which has the fcc structure with Fe atoms at all corners of the cubic unit cell (see figure 7(a)). The simulations use a single-scattering cluster model that is suitable for this application [28]. The spherical cluster has a radius of 30 Å, which includes a fluorescing Fe atom at the centre and approximately 10 000 scatterers. The lattice constant is that for the ordered phase of $FeNi_3$ (3.55 Å). The non-resonant scattering factors $f_0\left(\theta_R^{\boldsymbol{k}}\right)$ were calculated from the standard tables [43]. The anomalous dispersion corrections for Ni were calculated from the experimental absorption coefficient of Ni [44] by using the computer code developed by Newville and Cross [45], while the slowly varying values for Fe were taken from another database [35]. A hologram at each of the three energies shown in figure 6 was calculated over the full solid angle of 4π steradians with a step width of 3° for both polar and azimuthal scans. Although it is usually impossible to measure a hologram over the full solid angle, in many cases, a measured hologram can be extended over the full solid angle by using the symmetry of the crystal (e.g. inversion symmetry, as is the case for $FeNi_3$), thereby improving the image resolution along the vertical direction. The image resolution and the maximum radius within which the image is reliable for this $\boldsymbol{k}$-space sampling are expected to be approximately 0.7 and 18 Å, respectively [28].

Three-dimensional atomic images have been reconstructed from the theoretical holograms by both the original MEXH algorithm and the RXFH algorithm based on equation (10), and

are shown in figures 7(b) and (c), respectively. The MEXH image in figure 7(b) yields five Fe peaks and four Ni peaks at the respective sites of these atoms on each crystal plane. The atomic peaks for Fe denoted as Fe_2 in the figure appear to be split into two parts. Such peak splitting is often observed in single-energy holography, and since we have used only three energies here, this could explain this type of image aberration. Nonetheless, all the atomic peaks observed are fairly well resolved, and their positions are close to the true positions, but of course without clear distinction between Fe and Ni. On the other hand, in figure 7(c), using the contrasting mechanism of RXFH, the atomic peaks for Fe are almost completely suppressed, while the peaks for Ni are clearly visible. In figures 7(d) and (e), a more detailed comparison between MEXH and RXFH is presented. This shows that RXFH can very effectively discriminate between two species with close atomic numbers and reveals the chemical order around the fluorescing atom. The maximum image intensity for Ni in RXFH is approximately 18% of that in MEXH. This confirms the previous argument, based on the dispersion curve of f_1, that the experimental challenge associated with RXFH can be comparable to that in MEXH for light elements such as C, N and O, and that RXFH should thus be feasible with current third-generation synchrotron radiation capabilities.

Thus, the RXFH scheme has been demonstrated theoretically and awaits demonstration experimentally. To enhance the resonant effects and suppress the contributions from non-resonant species, the choice of incident x-ray energies is extremely important. From the experimental point of view, the signal-to-noise ratio of the hologram is the most important factor. The accuracy in tuning x-ray energies is also critical. Our simulations show that RXFH should be successful in selectively imaging a single species of atom in a compound. Therefore, not only the atomic arrangement but also the chemical order around each atom can be determined by comparing the reconstructed images via MEXH and RXFH. This technique should be particularly useful for studying such issues as the structural environment of dopant atoms in compound semiconductors and complex oxides, and the order–disorder transition of alloys; and it may ultimately find use in studies of active sites in biological molecules.

Acknowledgments

This work was supported in part by the Director, Office of Science, Office of Basic Energy Sciences, Division of Materials Sciences, of the US Department of Energy under contract no DE-AC03-76SF00098. SO also acknowledges the support of the Japan Society for the Promotion of Science (grant no JSPS-RFTF 98R14101).

References

[1] Szöke A 1986 *Short Wavelength Coherent Radiation: Generation and Applications (AIP Conf. Proc. No. 147)* ed D T Attwood and J Boker (New York: AIP) p 361
[2] Barton J J 1988 *Phys. Rev. Lett.* **61** 1356
[3] Barton J J 1991 *Phys. Rev. Lett.* **67** 3106
Barton J J and Terminello L J 1991 *Structure of Surfaces* vol 3, ed S Y Tong, M A Van Hove, X Xide and K Takayanagi (Berlin: Springer) p 107
Tong S Y, Li H and Huang H 1991 *Phys. Rev. Lett.* **67** 3102
[4] Tonner B P, Han Z L, Harp G R and Saldin D K 1991 *Phys. Rev.* B **43** 14 423
[5] Terminello L J, Barton J J and Lapiano-Smith D A 1993 *Phys. Rev. Lett.* **70** 599
[6] Tong S Y, Li H and Huang H 1995 *Phys. Rev.* B **51** 1850
Wu H and Lapeyre G J 1995 *Phys. Rev.* B **51** 14 549
[7] Len P M, Denlinger J D, Rotenberg E, Kevan S D, Tonner B P, Chen Y, Van Hove M A and Fadley C S 1999 *Phys. Rev.* B **59** 5857
[8] Saldin D K, Harp G R and Chen X 1993 *Phys. Rev.* B **48** 8234

[9] Wei C M, Hong I H and Chou Y C 1994 *Surf. Rev. Lett.* **1** 335
[10] Saldin D K and de Andres P L 1990 *Phys. Rev. Lett.* **64** 1270
Reuter K, Vamvakas J A, Saldin D K, Blum V, Ott M, Wedler H, Döll R and Heinz K 1998 *Phys. Rev.* B **58** 4102
[11] Tegze M and Faigel G 1991 *Europhys. Lett.* **16** 41
Len P M, Thevuthasan S, Fadley C S, Kaduwela A P and Van Hove M A 1994 *Phys. Rev.* B **50** 11 275
[12] Gog T, Len P M, Materlik G, Bahr D, Sanchez-Hanke C and Fadley C S 1996 *Phys. Rev. Lett.* **76** 3132
[13] Korecki P, Korecki J and Ślezak T 1997 *Phys. Rev. Lett.* **79** 3518
[14] Bompadre S G, Petersen T W and Sorensen L B 1999 *Phys. Rev. Lett.* **83** 2741
[15] Kaduwela A P, Wang Z, Thevuthasan S, Van Hove M A and Fadley C S 1994 *Phys. Rev.* B **50** 9656
[16] Omori S, Nihei Y, Rotenberg E, Denlinger J D, Kevan S D, Tonner B P, Van Hove M A and Fadley C S *Phys. Rev. Lett.* at press
[17] Omori S, Zhao L, Marchesini S, Van Hove M A and Fadley C S *Phys. Rev.* B at press
[18] Luh D-A, Miller T and Chiang T-C 1998 *Phys. Rev. Lett.* **81** 4160
[19] Greber T and Osterwalder J 1996 *Chem. Phys. Lett.* **256** 653
[20] Sinkovic B, Hermsmeier B D and Fadley C S 1985 *Phys. Rev. Lett.* **55** 1227
Hermsmeier B D, Osterwalder J, Friedman D J and Fadley C S 1989 *Phys. Rev. Lett.* **62** 478
Hermsmeier B, Osterwalder J, Friedman D J, Sinkovic B, Tran T and Fadley C S 1990 *Phys. Rev.* B **42** 11 895
[21] Tober E D, Palomares F J, Ynzunza R X, Denecke R, Morais J, Wang Z, Biino G, Liesegang J, Hussain Z and Fadley C S 1998 *Phys. Rev. Lett.* **81** 2360
[22] Starke K, Kaduwela A P, Liu Y, Johnson P D, Van Hove M A, Fadley C S, Chakarian V, Chaban E E, Meigs G and Chen C T 1996 *Phys. Rev.* B **53** R10 544
[23] Fadley C S *et al* 1997 *Prog. Surf. Sci.* **54** 341
[24] Chen Y, García de Abajo F J, Chassé A, Ynzunza R X, Kaduwela A P, Van Hove M A and Fadley C S 1998 *Phys. Rev.* B **58** 13 121
[25] Timmermans E M E, Trammell G T and Hannon J P 1994 *Phys. Rev. Lett.* **72** 832
Timmermans E M E, Trammell G T and Hannon J P 1993 *J. Appl. Phys.* **73** 6183
[26] Fadley C S 1993 *Surf. Sci. Rep.* **19** 231
[27] Omori S, Kozakai T and Nihei Y 1999 *Surf. Rev. Lett.* **6** 1085
[28] Len P M 1997 *PhD Thesis* University of California, Davis
[29] Wider J, Baumberger F, Sambi M, Gotter R, Verdini A, Bruno F, Cvetko D, Morgante A, Greber T and Osterwalder J 2001 *Phys. Rev. Lett.* **86** 2337
[30] Daimon H 2001 *Phys. Rev. Lett.* **86** 2034
[31] Daimon H, Nakatani T, Imada S, Suga S, Kagoshima Y and Miyahara T 1993 *Japan. J. Appl. Phys.* **32** 1480
Westphal C, Kaduwela A P, Fadley C S and Van Hove M A 1994 *Phys. Rev.* B **50** 6203
Kaduwela A P, Xiao H, Thevuthasan S, Fadley C S and Van Hove M A 1995 *Phys. Rev.* B **52** 14 297
Ynzunza R X *et al* 2000 *J. Electron Spectrosc.* **106** 7
[32] Oelsner A and Fecher G 1999 *J. Electron Spectrosc. Relat. Phenon.* **101–3** 455
[33] Gabor D 1948 *Nature* **161** 777
[34] Tegze M and Faigel G 1996 *Nature* **380** 49
Kawai J, Hayashi K, Yamamoto T, Hayakawa S and Gohshi Y 1998 *Anal. Sci.* **14** 903
Hiort T, Novikov D V, Kossel E and Materlik G 2000 *Phys. Rev.* B **61** R830
[35] http://www-cxro.lbl.gov/optical_constants/asf.html
[36] Len P M, Fadley C S and Materlik G 1997 *X-ray and Inner-Shell Processes: 17th Int. Conf. (AIP Conf. Proc. No. 389)* ed R L Johnson, H Schmidt-Boeckering and B F Sonntag (New York: AIP) pp 295–319
[37] Faigel G and Tegze M 1999 *Rep. Prog. Phys.* **62** 355–93
[38] Tegze M, Faigel G, Marchesini S, Belakhovsky M and Ulrich O 2000 *Nature* **407** 38
[39] Marchesini S, Schmithüsen F, Tegze M, Faigel G, Calvayrac Y, Belakhovsky M, Chevrier J and Simionovici A S 2000 *Phys. Rev. Lett.* **85** 4723
[40] Hayashi K, Yamamoto T, Kawai J, Suzuki M, Goto S, Hayakawa S, Sakurai K and Gohshi Y 1998 *Anal. Sci.* **14** 987
[41] Marchesini S, Ulrich O, Faigel G, Tegze M, Belakhovsky M and Simionovici A S 2001 *Nucl. Instrum. Methods* A **457** 601
[42] Attwood D T 1999 *Soft X-rays and Extreme Ultraviolet Radiation* (Cambridge: Cambridge University Press) pp 52, 39
[43] C H Macgillavry, G D Rieck and K Lonsdale (ed) 1968 *International Tables for X-ray Crystallography* vol 3 (Birmingham: Kynoch) p 201
[44] http://ixs.csrri.iit.edu/database/
[45] http://cars.uchicago/~newville/dafs/difkk/

JOURNAL OF APPLIED PHYSICS **103**, 07C519 (2008)

Probing multilayer spintronic structures with photoelectron and x-ray emission spectroscopies excited by x-ray standing waves (invited)

S.-H. Yang,[1] B. C. Sell,[2,3,a)] and C. S. Fadley[2,3,b)]
[1]*IBM Almaden Research Center, San Jose, California 95120, USA*
[2]*Physics Department, University of California Davis, Davis, California 95616, USA*
[3]*Materials Sciences Division, Lawrence Berkeley National Laboratory, Berkeley, California 94720, USA*

(Presented on 9 November 2007; received 9 October 2007; accepted 10 November 2007; published online 13 March 2008)

We discuss a newly developed x-ray standing-wave/wedge (swedge) method for probing the composition, magnetization, and electronic densities of states in buried interfaces and layers in spintronic nanostructures. In work based on photoemission, this method has permitted determining concentration and magnetization profiles through giant magnetoresistive (GMR) and magnetic tunnel junctions structures, as well as individual layer densities of states near the Fermi level in a tunnel junction. Using x-ray emission and resonant inelastic x-ray scattering for detection has permitted probing deeper layers and interfaces in a GMR structure. Various future applications of this method in nanomagnetism are suggested, including using more energetic hard x-ray standing waves so as to probe more deeply below a surface and standing-wave excitation in spectromicroscopy to provide depth sensitivity. © *2008 American Institute of Physics*. [DOI: 10.1063/1.2837481]

I. INTRODUCTION

Multilayer nanometer-scale structures are ubiquitous in current magnetic devices, and the detailed characteristics of the layers making them up, including the interfaces between layers, are often decisive as to ultimate functional properties. Buried layers and interfaces are thus crucial elements in such devices, but characterizing them fully presents unique challenges. Various microscopies such as scanning tunneling, atomic force, low energy electron without and with spin resolution, scanning transmission x-ray, zone-plate focused x-ray (XM), and photoelectron emission (PEEM) without and with spin resolution can provide high in-plane lateral resolution, and for XM and PEEM also element-specific resolution of structures, but most of these techniques tend to be very surface sensitive, and all have limited depth-resolving ability for buried structures. Soft x-ray scattering on and off resonant conditions provides the ability to vary the probing depth, but the scattered intensities must still be fit to x-ray optical simulations to derive depth-resolved information. Transmission electron microscopy with electron energy loss spectroscopy is perhaps the most direct method for looking in an element-specific way at layered structures and interfaces, but it is not nondestructive in requiring the sectioning of the sample, and is more limited in the range of chemical, magnetic, and bonding information available than a technique which could in some way make use of photoelectron or x-ray emission as the probing spectroscopies. The relatively newly developed standing-wave/wedge or swedge method that is the primary focus of this paper is such a technique, and we here discuss its applications to a few systems of interest in spintronics and summarize its advantages and disadvantages.[1–8]

The basic principle of the method is illustrated in Fig. 1, with some specific numbers for the first case studied: the Fe/Cr interface, a prototype system exhibiting giant magnetoresistance.[3] A well-focussed soft x-ray synchrotron radiation (SR) beam, in this case from the Berkeley Advanced Light Source, is tuned to be incident on a multilayer mirror at the first-order Bragg angle, thus leading to a high reflectivity and a strong standing wave above the mirror. If the bilayers making up the mirror, in this example consisting of B_4C and W, have an overall period d_{ML}, then simple geometric considerations lead to the period of the standing wave, as judged by the square of its electric field, also having a period of d_{ML}. On top of the mirror, the sample is grown, in this case as a wedge of Cr underneath a top layer of Fe of constant thickness. Since the x-ray beam size is much smaller than the wedge length and its resulting standing wave phase is fixed relative to the multilayer surface, scanning the sample along the wedge slope (the x direction in the figure) effectively scans the standing wave through the sample. Thus, photoelectron or x-ray emission signals from different atoms will exhibit oscillatory behavior that can be directly interpreted in terms of depth distributions, again with the aid of x-ray optical calculations, but in what we believe is a more direct way than is possible in the scattering measurements mentioned above.

II. APPLICATIONS USING STANDING-WAVE EXCITED PHOTOEMISSION

As a first example of the kind of results that can be obtained from such data, Fig. 2 shows both the depth profile of Fe and Cr concentrations and the depth profile of element-

a)Present address: Physics Department, Otterbein College, Westerville, OH 43081, USA.
b)Electronic mail: fadley@physics.ucdavis.edu.

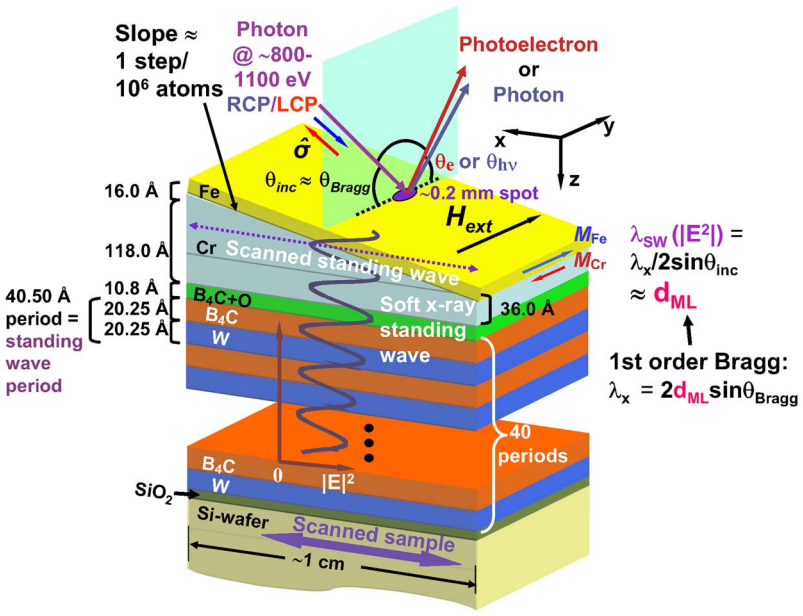

FIG. 1. (Color online) The basic geometry of the standing-wave/wedge ("swedge") method for probing buried layers and interfaces via photoelectron emission or x-ray emission, with some specific numbers relevant to the study in Ref. 3. Soft x rays are incident at the first-order Bragg angle for a multilayer mirror substrate of period d_{ML}, thus creating a strong standing wave above the mirror whose period is also d_{ML}. One layer of the multilayer sample is grown in a wedge profile, so that scanning the sample along the wedge slope (the x direction) also scans the standing wave through the sample. The polarization of the radiation can also be varied so as to carry out element-specific magnetic circular dichroism (MCD) measurements.

specific magnetizations for Fe and Cr that have been derived by measuring the Fe $2p$ and Fe $3p$, as well as the Cr $2p$ and Cr $3p$, photoelectron intensities and magnetic circular dichroism (MCD) effects.[2,3] From the intensity curves, the concentration profiles have been derived at the left, and from the dichroism curves, the magnetization profiles at the right, with accuracies in the parameters involved that are estimated to be $\sim \pm 2-3$ Å. From the relative magnitudes and signs of the MCD effects, it could also be concluded that Cr is weakly ferromagnetic just under the interface, but it is antiferromagnetically coupled to Fe.

As another example related to magnetic tunnel junctions (MTJs), Fig. 3 summarizes some photoemission data from a sample consisting of an Al_2O_3 wedge, a layer of CoFe, and a layer of CoFeB, with a final protective cap of Al_2O_3. Figure 3(a) shows the B $1s$ spectrum, which is split into two components by what is probably a large chemical shift. Whatever the source of these two components A and B, they can be verified as two chemically and spatially distinct species by looking at either the standing wave scans of the two intensities in Fig. 3(c) or another type of scan in Fig. 3(b) in which the x position is fixed and the sample is simply rotated around the equivalent of the x axis in Fig. 1 (a type of rocking curve). The two components have markedly different behaviors in either data set, and the fact that their two oscillatory patterns in Fig. 3(c) exhibit a phase shift relative to one another of about 7 Å immediately suggests that their mean depths are different by about the same magnitude. Considering the direction of the wedge slope further implies that peak B represents atoms closer to the surface. A more precise analysis of both sets of data in fact yields the concentration profiles responsible for these two peaks indicated in Fig.

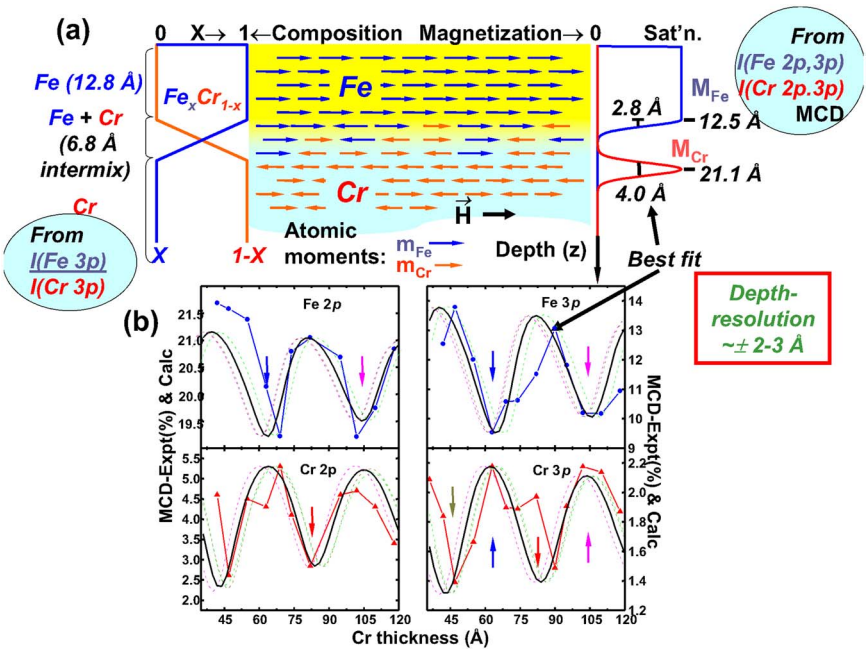

FIG. 2. (Color online) (a) The concentration profiles and element-specific magnetization profiles of Fe and Cr through the Fe/Cr interface of the sample shown in Fig. 1 that have been derived from Fe $2p$ and Fe $3p$ intensities and MCD measurements, respectively. (b) A summary of the Fe and Cr MCD data used to derive the magnetization profiles. The solid curve is the best fit from many different choices of parameters describing the magnetization variation of either Fe or Cr through the interface. The dashed curves and dotted curves represent several choices of parameters that were used to estimate the error limits of $\sim \pm 2-3$ Å (from Ref. 3).

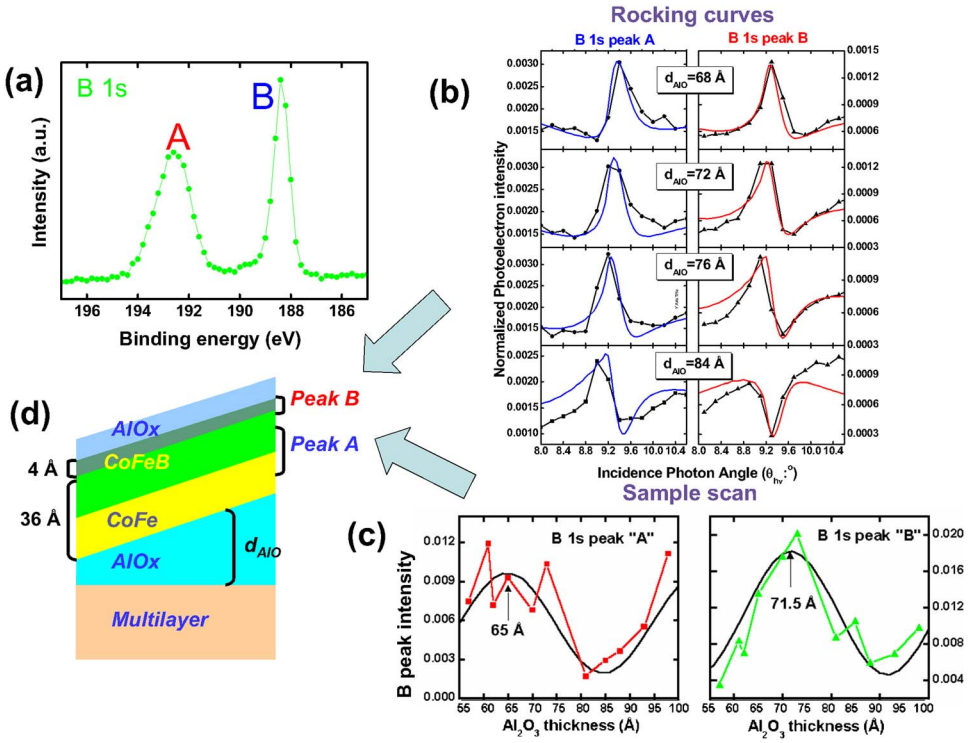

FIG. 3. (Color online) (a) The boron 1*s* spectrum from a CoFeB layer on top of a sample with the configuration shown in (d). (b) Rocking curves of the intensity of the two components A and B in (a), obtained by varying the x-ray incidence angle around the multilayer Bragg angle. The experimental points are connected by straight lines. The smooth curves represent best fits to the data, as derived from a fit of x-ray optical calculations to the data. (c) The variation of the intensities of peaks A and B as the standing wave is scanned through the sample by moving the sample in the *x* direction. The curve format is the same as in (b). (d) The distribution of the two types of boron in the sample, as derived from the best fits of x-ray optical calculations to the data (Ref. 8).

3(d), and the conclusion that some of the B in the CoFeB layer has segregated out into the interface between CoFeB and the Al_2O_3 capping layer.

For the same MTJ sample type as in Fig. 3, it has also been possible to use several valence-band spectra obtained as the standing wave is scanned through the sample to yield layer-resolved densities of states, and in particular, to provide a microscopic understanding of the marked increase in tunnel magnetoresistance (TMR) when the CoFe layer is decreased in thickness d_{CoFe} from 25 to 15 Å.[5] Figure 4 summarizes these results, with parts (a) and (b) showing a typical valence spectrum for the two different CoFe thicknesses, after having been self-consistently fit with five components A–E. Eleven such spectra were measured for a succession of standing wave positions, and the insets in Figs. 4(a) and 4(b) show the variation in relative intensity of the E component nearest the Fermi level (as measured with respect to the sum of the C and D components), compared to an x-ray optical calculation of the relative importance of emission from FeCo and FeCoB. There is a clear correlation between the intensity of E and the degree to which the standing wave is localized on FeCo. Beyond this, self-consistently analyzing all eleven

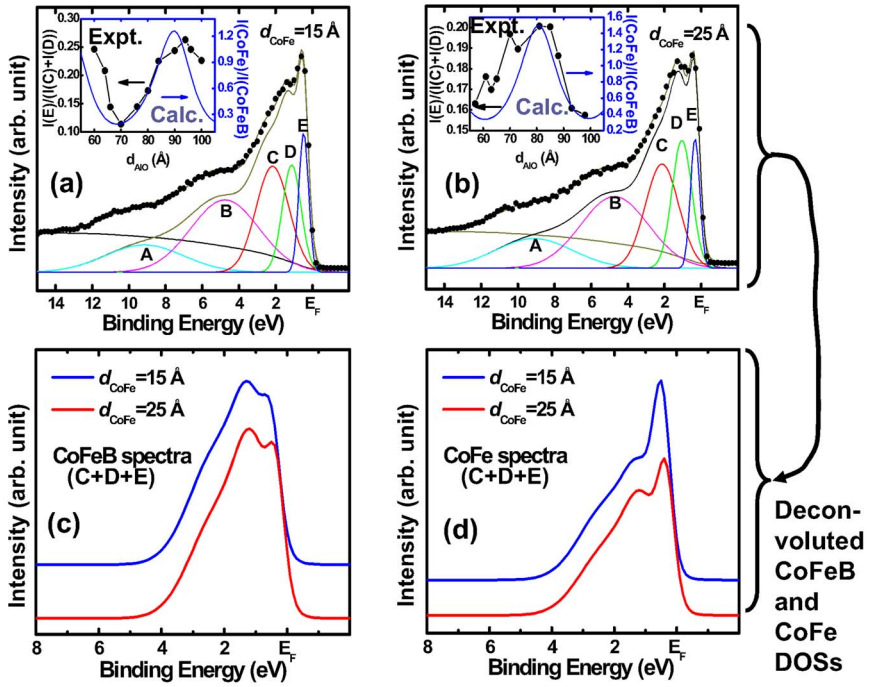

FIG. 4. (Color online) Extraction of layer-specific densities of states in a magnetic tunnel junction sample. [(a) and (b)] Typical valence-band spectra at a certain standing wave position for two different thicknesses of a CoFe layer, and with decomposition of the spectrum into five components by peak fitting. The insets show the measured relative intensity of peak E nearest the Fermi level versus an x-ray optical calculation of the relative intensity of the CoFe layer compared to the overlying CoFeB layer. [(c) and (d)] The layer-specific densities of states of CoFeB and CoFe, respectively, for two different thicknesses of the CoFe layer. Note the much enhanced peak near the Fermi level for CoFe with a thickness of 15 Å (from Ref. 5).

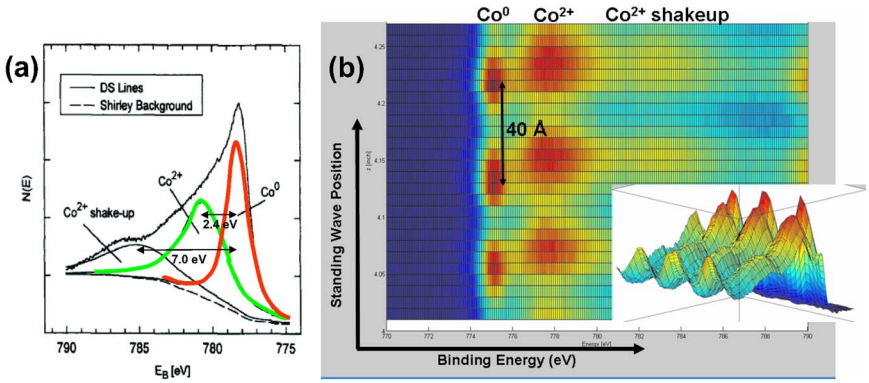

FIG. 5. (Color online) (a) A Co $2p$ spectrum from oxidized Co, as obtained from the literature (Ref. 9), indicating the three features expected: one from Co^0 and two from Co^{2+} (a main peak and a broad shakeup or screening satellite). (b) The effect of scanning the standing wave through the sample on the Co $2p$ spectrum. Note the obvious phase shift between the Co^0 and Co^{2+} peaks (from Ref. 8).

spectra with the assumption that each of the two layers has a distinct and constant density of states yields the layer-resolved densities of states shown in Figs. 4(c) and 4(d). These results finally permit concluding that the enhanced TMR for 15 Å of FeCo compared to 25 Å can be linked to a significantly higher density of states at the Fermi level, which is further reasoned to be spin polarized, and also to the fact that the FeCo is thought to go from polycrystalline to amorphous when its thickness is decreased from above 25 to 15 Å.[5]

As a final type of MTJ structure studied using the swedge method with photoelectron emission, a structure consisting of an Al_2O_3 wedge covered by a constant-thickness Co layer and a Ru cap has been studied.[8] For one type of sample produced with a synthetic procedure involving a 30 s final plasma oxidation of the Al_2O_3 just before deposition of the Co, the Co is found via Co $2p$ chemical shift analysis to be highly oxidized. Figure 5(a) shows a reference Co $2p$ spectrum from the literature, with one sharp feature from metallic Co (Co^0) and two peaks from Co oxide (Co^{2+}).[9] We find the same spectral features, but the swedge measurements show that the oxide is situated on average above the metallic Co, rather than below it and adjacent to the Al_2O_3. Figure 5(b) summarizes a standing wave scan of the Co $2p$ spectrum and, in the same sense that the two boron species A and B in Fig. 3(a) have a phase shift in Fig. 3(c), so does the single Co metal component have a phase shift of about 16 Å relative to the two components from Co oxide in the Co^{2+} state. This shift is in turn in a direction indicating that the oxide is nearer the surface. Beyond this, the oscillatory patterns seen for the various core level intensities of different atoms from this sample, as plotted in Fig. 6, yield a family of phase shifts which can be analyzed to determine depth distributions. For example, O $1s$ is split into what appears to be two metal-oxide components, one that is in phase with Co oxide and nearer to the surface, and one connected with Ru that is below the surface. The metallic Co signal also seems to come from not very far below the Ru on average. These results thus point to a very strong intermixing and/or island formation in the Co and Ru layers, with the relative weakness of the Ru oscillations also suggesting that it has distributed itself over depths that must be approaching the wavelength of the standing wave, which was in this case 40 Å. An approximate picture of the sample profile is shown in the inset of Fig. 6, and it is very different from what might have been supposed from the synthetic recipe.

III. APPLICATIONS USING STANDING-WAVE EXCITED X-RAY EMISSION

As a final development of this swedge method, we consider detecting photons emitted from the sample, either as normal x-ray emission spectroscopy (XES) or as the closely related experiment of resonant inelastic x-ray scattering (RIXS) in which the incoming photon energy is tuned to a strong absorption resonance, and the outgoing photons, at lower energies than the excitation, are measured. The fact that photons have much greater penetration and escape depths than electrons of comparable energies makes this type of measurement capable of looking much more deeply into multilayer structures, and we will also show that this permits characterizing both the top and bottom interfaces of a given layer. In photoemission measurements, the strong attenuation of the emission from a given layer due to inelastic electron scattering during escape tends to bias the data strongly toward seeing only the top interface.

This additional type of photon-out measurement is again illustrated for the case of the Fe/Cr interface, but in this case, the sample consisted of an Fe layer sandwiched between an underlying Cr wedge and an overlying Al_2O_3 capping layer.[7] There are thus two interfaces involved, Al_2O_3/Fe on top and Fe/Cr on the bottom. We have in particular looked at the Cr and Fe L x-ray spectra, as excited by a photon at the Fe $2p_{1/2}$ absorption edge, which yields a typical broad-scan spectrum, as shown in Fig. 7. The Fe L

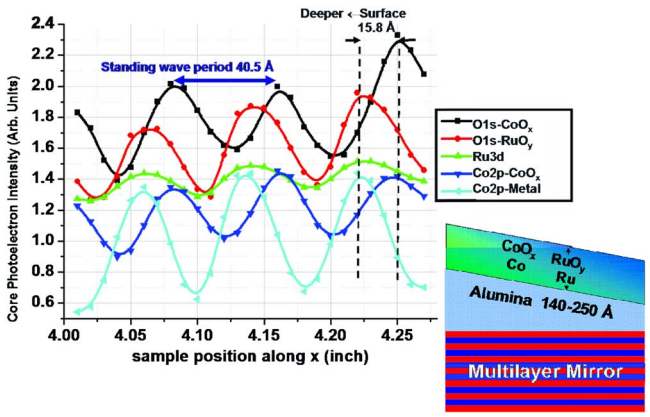

FIG. 6. (Color online) (a) The oscillatory intensity variations of different core-level photoelectron intensities as the standing wave is scanned through a sample with the configuration shown in (b). The different peaks involved are indicated (from Ref. 8).

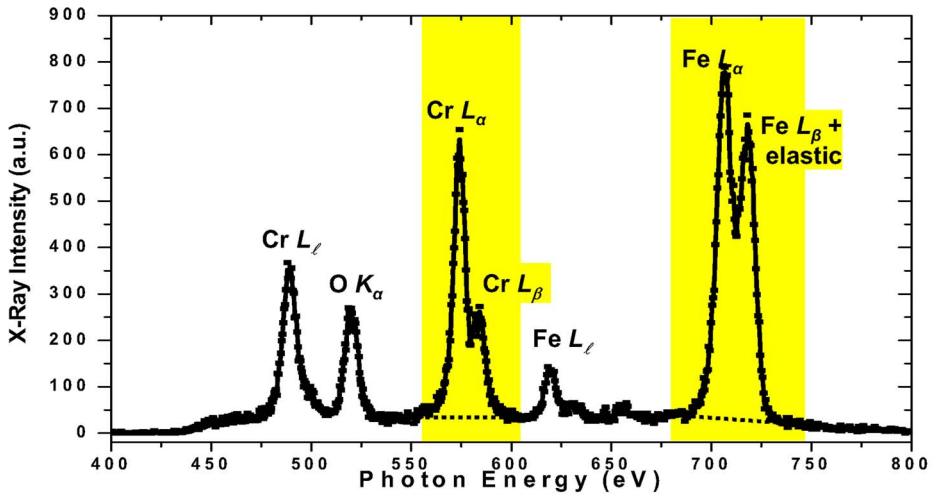

FIG. 7. (Color online) A scan of emitted x-ray intensity over a broad energy range encompassing O, Cr, and Fe soft x-ray emission processes. The exciting x ray, which is elastically scattered into the spectrometer, is very close to the energy of Fe L_β and contributes about 40% of the intensity above the dashed linear background of the combined Fe L_α+Fe L_β that is plotted in Fig. 8 (from Ref. 7).

spectra are thus strictly speaking RIXS emission, but the Cr L spectra would be normal XES. Other x rays are also emitted from Cr, Fe, and O, as indicated in this figure.

Figure 8 shows the oscillatory patterns associated with Fe L emission; (a) as summed over excitation with left and right circularly polarized radiation, (b) as the difference between left and right, and (c) as twice the ratio of these two quantities, which is the MCD signal. Over three cycles of the standing wave have passed through the Fe layer, and all three of the quantities in this figure exhibit clear oscillations of the order of 25%, 15%, and 10% around their mean values, respectively. As a first conclusion connected with these data, the fact that there is a nonconstant and oscillatory MCD signal can be shown rigorously to require that the Fe atoms contributing to it do not have the same strength in the interface regions.[7] The slight phase shift between the summed intensity in (a) and the MCD signal in (c), which is about 3–4 Å in vertical standing wave position, and the greater asymmetry and width of the peaks in the MCD oscillations also indicates that the two Fe interfaces do not have the same magnetization profile.[7] The red curves in Fig. 8 are the result of an analysis involving a large number of x-ray optical calculations for different layers and interface geometries, with the resulting parameters between two layers i and j, constant-composition layer thicknesses t_{ij}, linear-gradient concentration interface thicknesses w_{ij}, and Gaussian-profile magnetization half widths g_{ij}, as shown in Fig. 9. Thus, the properties of both top and bottom interfaces have been determined via this analysis, something that would not be possible with photoelectron emission.

IV. FUTURE APPLICATIONS: HARD X RAYS AND MICROSCOPY

Finally, we comment briefly on two additional interesting developments that could permit the swedge method to study additional aspects of spintronic structures.

First is the idea of using much harder x rays for excitation of photoelectrons, going from soft x-rays in the 500–1000 eV regime up to 5 or 10 keV, in order to penetrate multilayer structures more deeply. There is presently growing activity in Europe and Japan in carrying out photoemission in this regime,[10,11] and some of these possibilities for studies of magnetism have already been discussed in a recent comprehensive review of x-rays in magnetism.[6] Among other things, it has been pointed out that standing waves above nanometer-scale multilayer mirrors should be even stronger in this higher-energy regime,[6,12] and thus more accurate characterizations of even deeper structures should be possible. In recent work that did not involve standing waves, such hard x-ray photoemission has in fact been used in connection with chemical shifts and local density calculations to study interface mixing in the Ni/Cu interface.[13] By using standing wave excitation, this type of characterization could be even more quantitatively carried out.

As a final possibility for the future, carrying out soft x-ray-excited XM or PEEM studies with standing-wave excitation could provide a type of direct depth sensitivity to these laterally resolving SR techniques, provided that a few standing wave cycles can be encompassed in a single microscope image. Some first encouraging measurements of this type have in fact recently been carried out.[14]

V. CONCLUDING REMARKS

The standing-wave/wedge method discussed here thus has demonstrated the ability to nondestructively determine buried-interface concentration profiles and element-specific magnetization profiles, as well as layer-specific densities of states in a variety of multilayer nanostructures of interest in spintronics. A limitation of the technique is that a suitable sample structure must be grown on a multilayer mirror of sufficient reflectivity, but there nonetheless seem to be a variety of systems for which this should be possible, and a range of applications areas, both in magnetism and other fields.[4] Both photoelectron emission and x-ray emission/inelastic scattering can be used as probes, with the latter providing greater bulk sensitivity and the ability to look at both the top and bottom interfaces of different layers. Using more energetic x rays will permit studying deeper layers and interfaces, and using soft x-ray standing waves for imaging with photoelectron microscopy may also permit adding depth resolution to this family of techniques.

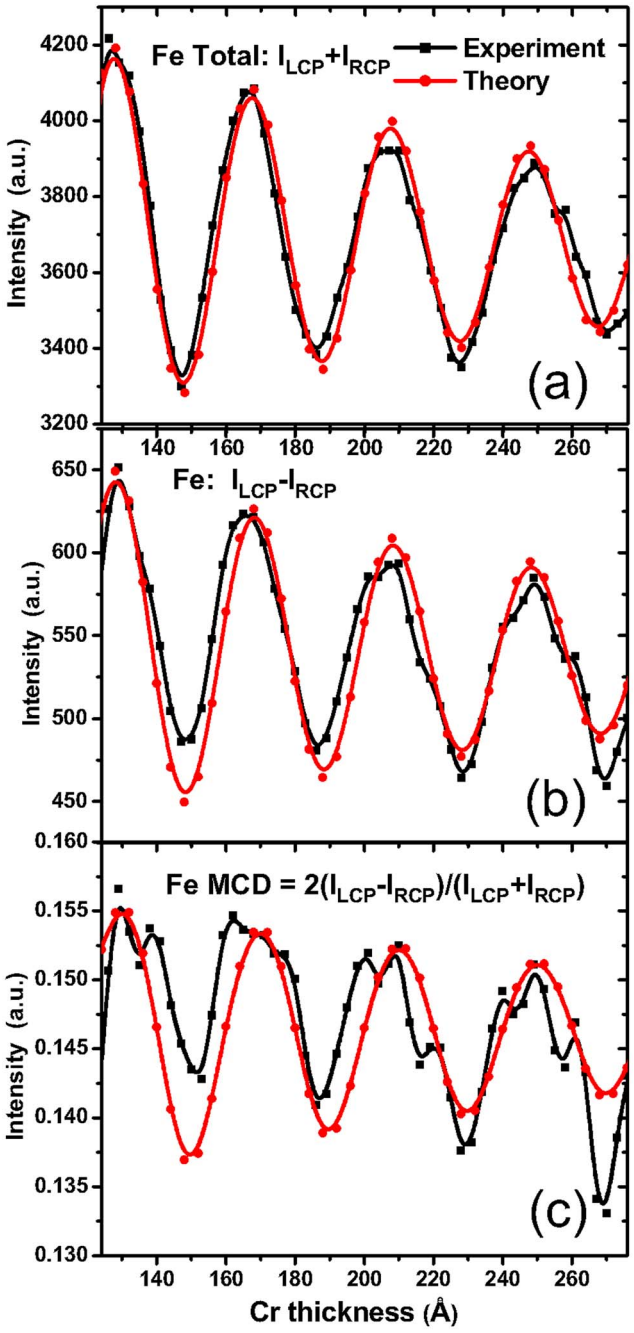

FIG. 8. (Color online) The effect of scanning the standing wave through an Al_2O_3/Fe/Cr trilayer on (a) the sum of the Fe L_α+Fe L_β intensities for excitation with right and left circular-polarized excitations, $I_{LCP}+I_{RCP}$, adjusted for the influence of the elastically scattered exciting intensity and on (b) the difference of Fe L_α+Fe L_β intensities, $I_{LCP}-I_{RCP}$. (c) The MCD derived from (a) and (b) via MCD=$2(I_{LCP}-I_{RCP})/(I_{LCP}+I_{RCP})$ (from Ref. 7).

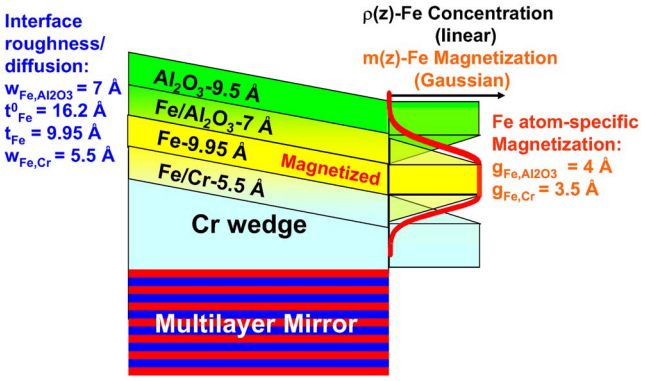

FIG. 9. (Color online) The final layer configuration derived from the data in Fig. 8, including the initial deposited thickness of layer i t_i^0, the thickness of layer i that has not been influenced by interface roughness or intermixing t_i, interface linear concentration parameters w_{ij}, and Gaussian atom-specific magnetization halfwidths g_{ij}, where i and j refer to the two layers involved (from Ref. 7).

ACKNOWLEDGMENTS

This work was supported by the Director, Office of Science, Office of Basic Energy Sciences, Materials Science and Engineering Division, U.S. Department of Energy under Contract No. DE-AC03-76SF00098. One of us (C.S.F.) also gratefully acknowledges the support of the Alexander von Humboldt Foundation and the Helmholtz Association during part of this work.

[1] S.-H. Yang, B. S. Mun, A. W. Kay, S.-K. Kim, J. B. Kortright, J. H. Underwood, Z. Hussain, and C. S. Fadley, Surf. Sci. Lett. **461**, L557 (2000).
[2] S.-H. Yang, B. S. Mun, A. W. Kay, S. K. Kim, J. B. Kortright, J. H. Underwood, Z. Hussain, and C. S. Fadley, J. Electron Spectrosc. Relat. Phenom. **114**, 1089 (2001).
[3] S.-H. Yang, B. S. Mun, N. Mannella, S.-K. Kim, J. B. Kortright, J. Underwood, F. Salmassi, E. Arenholz, A. Young, Z. Hussain, M. A. Van Hove, and C. S. Fadley, J. Phys.: Condens. Matter **14**, L406 (2002).
[4] S.-H. Yang, B. S. Mun, and C. S. Fadley, Synchrotron Radiat. News **17**, 24 (2004).
[5] S.-H. Yang, B. S. Mun, N. Mannella, A. Nambu, B. C. Sell, S. B. Ritchey, F. Salmassi, S. S. P. Parkin, and C. S. Fadley, J. Phys.: Condens. Matter **18**, L259 (2006).
[6] G. Srajer, L. H. Lewis, S. D. Bader, C. S. Fadley, E. E. Fullerton, A. Hoffmann, J. B. Kortright, K. M. Krishnan, S. A. Majetich, C. A. Ross, M. B. Salamon, I. K. Schuller, and T. C. Schulthess, J. Magn. Magn. Mater. **307**, 1 (2006).
[7] B. C. Sell, S.-H. Yang, M. Watanabe, B. S. Mun, L. Plucinski, N. Mannella, S. B. Ritchey, A. Nambu, J. Guo, M. W. West, F. Salmassi, J. B. Kortright, S. S. P. Parkin, and C. S. Fadley, J. Appl. Phys. (submitted).
[8] B. C. Sell, Ph.D. thesis, UC Davis, 2007; B. C. Sell, S.-K. Yang, and C. S. Fadley (unpublished).
[9] B. Klingenberg, F. Grellner, D. Borgmann, and G. Wedler, Surf. Sci. **283**, 13 (1997).
[10] *Photoemission with Hard X-Rays*, edited by J. Zegenhagen and C. Kunz, special issue of Nucl. Instrum. Methods Phys. Res. A **547** (2005); C. S. Fadley, *ibid.* **547**, 24 (2005).
[11] Program and Abstracts of Recent International Workshop on Hard X-Ray Photoemission (HAXPES06), Spring8, Japan (unpublished) (http://haxpes2006.spring8.or.jp/program.html).
[12] C. S. Fadley, Nucl. Instrum. Methods Phys. Res. A **547**, 24 (2005).
[13] E. Holmstrom, W. Olovsson, I. A. Abrikosov, A. M. N. Niklasson, B. Johansson, M. Gorgoi, O. Karis, S. Svensson, F. Schafers, W. Braun, G. Ohrwall, G. Andersson, M. Marcellini, and W. Eberhardt, Phys. Rev. Lett. **97**, 266106 (2006).
[14] F. Kronast, A. Keiser, C. Wiemann, D. Buergeler, R. Schreiber, H. Dürr, C. Schneider, and C. S. Fadley (unpublished).